

Dual-Purpose CuFe₂O₄-rGO-Based Nanocomposite for Asymmetric Flexible Supercapacitors and Catalytic Reduction of Nitroaromatic Derivatives

Priyanka Makkar, Debika Gogoi, Debmalya Roy, and Narendra Nath Ghosh*

Cite This: *ACS Omega* 2021, 6, 28718–28728

Read Online

ACCESS |



Metrics & More

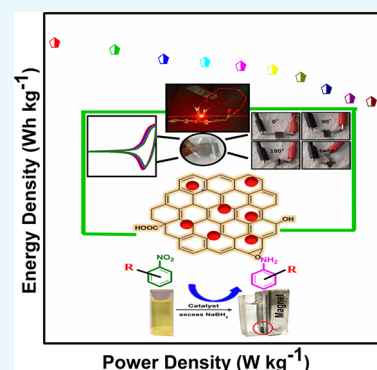


Article Recommendations



Supporting Information

ABSTRACT: Energy storage and environmental pollution are two major global concerns in today's scenario. As a result of the momentous exhaustion of fossil fuels, the generation of energy from renewable sources is gaining immense importance. However, the irregular availability of energy from these renewable sources is the major encounter to achieve sustainable energy harvesting technology, yielding efficient but continuous and reliable energy supplies. Apart from the requirement of state-of-the-art heavy-duty technologies such as transportation, defense, etc., in the modern lifestyle to fulfill the demand for flexible electronic devices, the development of high-performance mechanically flexible all-solid-state supercapacitors is increasing massively. On the other hand, to cater to the need for accessibility of clean water for healthy lives, several technologies are evolving to treat wastewater and groundwater. Hence, the development of efficient catalysts for destroying water pollutants is an attractive approach. Considering these two crucial facets, in this paper, we have demonstrated the multifunctional features of a CuFe₂O₄-rGO nanocomposite, which was exploited to fabricate a high-performance mechanically flexible all-solid-state asymmetric supercapacitor and simultaneously used as an efficient but easily recoverable catalyst for the transformation of different nitroaromatic compounds. We have also demonstrated the conversion of trifluralin (a herbicide), which is present in the water body as a pollutant, to its corresponding amine derivatives, which can be utilized in the preparation of important pharmaceutical products.



1. INTRODUCTION

The demand for developing multifunctional materials has gained immense attention from the scientific community across the globe for their applicability in various fields such as flexible supercapacitors (SCs), catalysis, sensors, etc. The multifunctional materials can be strategically designed by combining different materials with suitable properties to form a hybrid material to satisfy previously unfeasible performance metrics. In such a scenario, nanocomposites composed of graphene decorated with ferrite nanoparticles are eminently fascinating nanocomposites.^{1–3} In the present study, we have demonstrated the multifunctional nature of a CuFe₂O₄-rGO nanocomposite by using it in the construction of an all-solid-state flexible asymmetric supercapacitor device and a catalyst for the reduction of various nitroaromatic compounds.

Supercapacitors have procured increasing recognition owing to their high power density, long life, etc. Several review papers are available where fundamentals of SCs, categories of SC devices, different types of electrode materials, electrolytes, electrochemical reactions involved, fabrication of SCs, etc., have been discussed in detail.^{4–7} Among various supercapacitors, high-performance all-solid-state flexible supercapacitors have acquired immense academic and technological attention to satisfy the demand for compact, flexible, and wearable electronic products. Legerity and superior electro-

chemical performance have led to the improved miniaturization and wearability of these flexible devices.^{8–10}

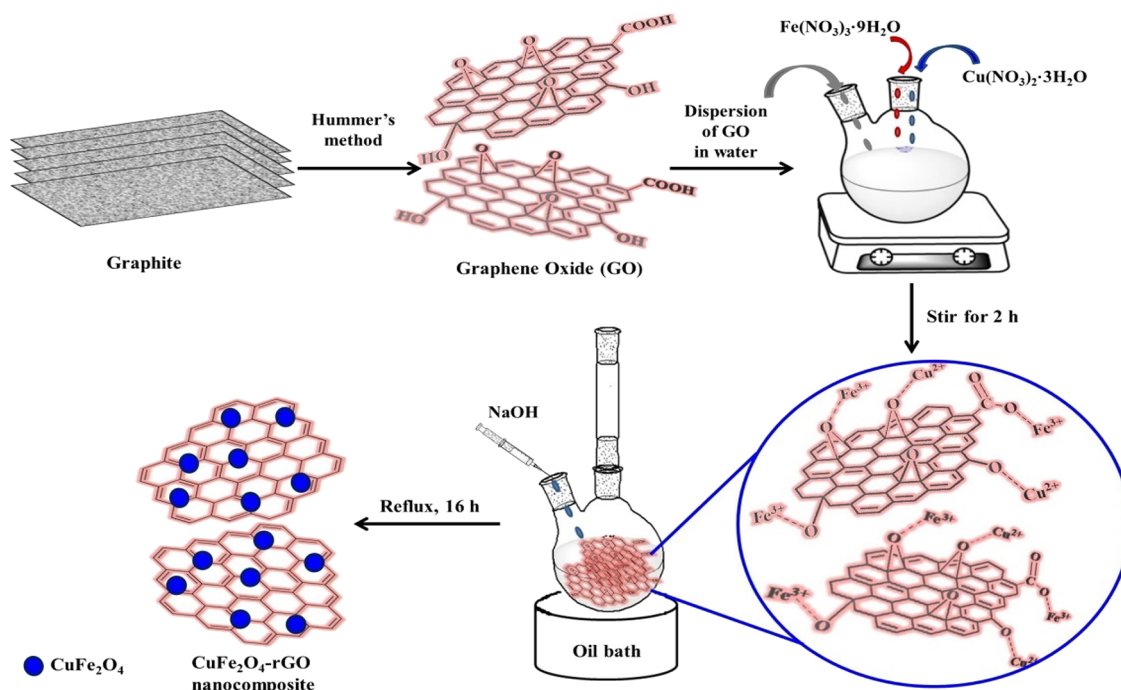
In the current status, supercapacitors, particularly symmetric SCs, suffer from inferior energy density (usually lesser than 10 Wh kg⁻¹).^{11,12} To surmount the impediments associated with the symmetric SC devices, the development of asymmetric supercapacitor (ASC) devices has become an alluring approach. The asymmetric supercapacitors augment the working potential by assembling two different positive and negative electrodes operating in different working voltage regions for the fabrication of a high-performance supercapacitor.^{4,5,13,14} This stimulates to complement the performance of the device in terms of energy density, power density, etc. With the electrode materials being the keystone for fabricating the supercapacitors, concocting asymmetric supercapacitors (ASCs) by decisively fusing the suitable electric double-layer capacitor (EDLC) and pseudocapacitive materials is a constructive approach.

Received: June 28, 2021

Accepted: October 11, 2021

Published: October 19, 2021



Scheme 1. Schematic Presentation of the Preparation of a CuFe_2O_4 -rGO Nanocomposite

Our previous investigations showed that the CuFe_2O_4 -rGO nanocomposite exhibited an impressive specific capacitance (C_s) value of 797 F g^{-1} at a current density of 2 A g^{-1} measured in a three-electrode setup, and this setup also demonstrates $\sim 92\%$ retention of C_s even after 2000 cycles.¹⁵ However, as the three-electrode measurements convey the electrochemical properties of the electrode materials only, a two-electrode assembly is needed to evaluate the performance of an SC device. The impressive features of the CuFe_2O_4 -rGO nanocomposite, realized from the three-electrode measurements, decisively endorse that we should explore the usage of this nanocomposite as the electrode material for the fabrication of high-performance ASC devices.

To manifest the multifunctional aspect of the CuFe_2O_4 -rGO nanocomposite, we have also appraised its catalytic performance toward the reduction of various nitroaromatic compounds. We have chosen this reaction because according to U.S. Environmental Production Agency, nitroaromatic compounds are highly toxic and act as major water pollutants. Traces of nitroaromatic compounds are commonly present in the wastewater discharged from the industries producing pesticides, herbicides, paint, wood preservatives, dyes and pigments, etc.,^{16,17} and are causing harm to both humans as well as other living species.¹⁸ Moreover, most of the nitroanilines and nitrophenols are neurotoxic and can damage the cardiovascular system.^{19,20} Several researchers have developed different strategies to remove nitroaromatic compounds from the wastewater such as catalytic moist air oxidation, catalytic reduction, photocatalytic degradation, electrolytic reduction, etc.^{17,19} Catalytic reduction of organic nitro compounds to their corresponding amino products is a very exciting methodology because the resulting products, i.e., the aromatic amino compounds, are industrially important intermediates in the manufacture of lubricants, corrosion inhibitors, analgesic drugs, polymers, etc.^{21–23} For this purpose, the reduction of nitroaromatic compounds in the presence of NaBH_4 in an aqueous medium is one of the widely

used methods due to its simplicity, high efficiency, cost-effectiveness, and eco-friendliness.^{19,24–26}

In our previous investigations, we have studied the catalytic activity of CuFe_2O_4 -rGO toward the reduction of 4-nitrophenol to 4-aminophenol, which revealed its remarkably high catalytic activity by completing the reaction within a very short duration ($\sim 4 \text{ min}$) with a high apparent rate constant ($k_{\text{app}} = 17.2 \times 10^{-3} \text{ s}^{-1}$).¹⁵ The phenomenal catalytic performance of the CuFe_2O_4 -rGO nanocomposite persuaded us to appraise this nanocomposite as a catalyst for the reduction of a variety of nitroaromatic compounds and also the toxic herbicide trifluralin.

Hence, in the present work, we have illustrated the multifunctional aspect of the CuFe_2O_4 -rGO nanocomposite by (i) constructing a high-performance all-solid-state flexible asymmetric supercapacitor device employing the CuFe_2O_4 -rGO nanocomposite as the cathode and rGO as the anode. This device exhibited excellent performance in terms of specific capacitance, energy density, power density, long cycling life, and safety (energy density of 38 Wh kg^{-1} at a power density of 2600 W kg^{-1} , along with excellent cycling performance ($\sim 97\%$ after 10,000 cycles)), which is superior to the commercial supercapacitor devices. These exceptional performances endorse the competency of this constructed ASC device for cutting-edge technology including modern wearable electronics. (ii) Employing the CuFe_2O_4 -rGO nanocomposite as a highly competent catalyst for the reduction reaction of varieties of nitroaromatic compounds and trifluralin (a toxic herbicide) to their corresponding amino derivatives, where the reaction completes within 2–4 min. The connotation of this catalysis reaction lies in its environment as well as commercial interest.

2. RESULTS AND DISCUSSION

2.1. Formation and Structural Characterizations of CuFe_2O_4 -rGO.

A “one-pot” synthesis process was acquired to synthesize the CuFe_2O_4 -rGO nanocomposite. In our previous

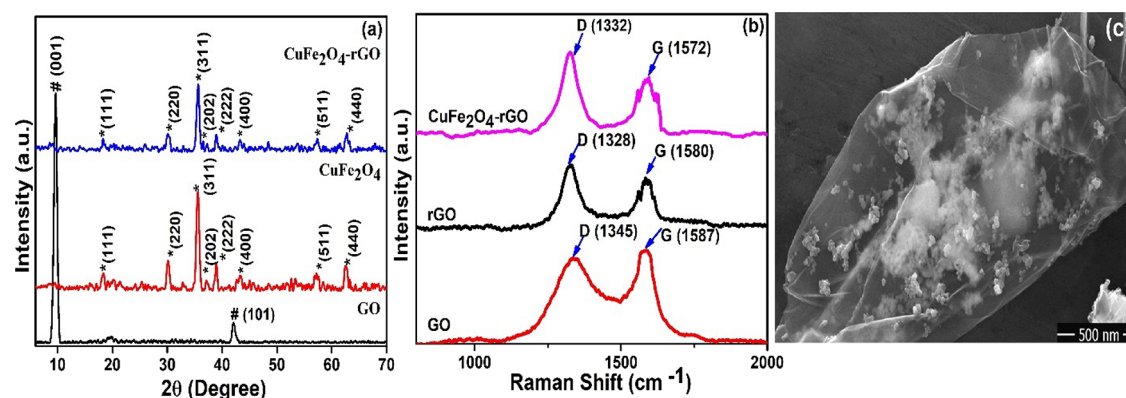


Figure 1. (a) XRD spectra, (b) Raman pattern of GO, rGO, and CuFe₂O₄-rGO nanocomposites, and (c) FESEM image of a CuFe₂O₄-rGO nanocomposite.

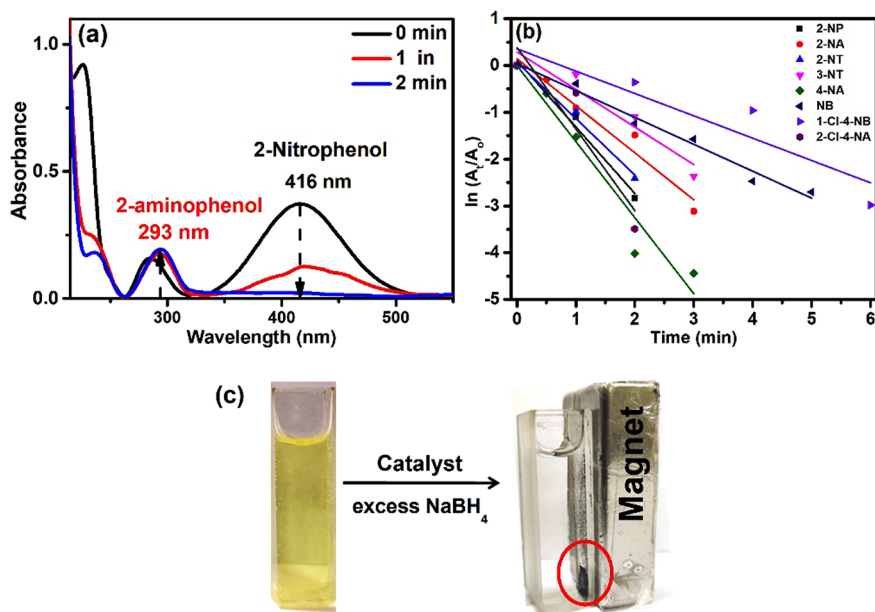
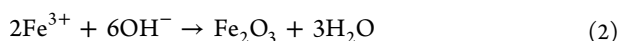
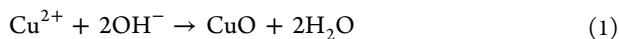


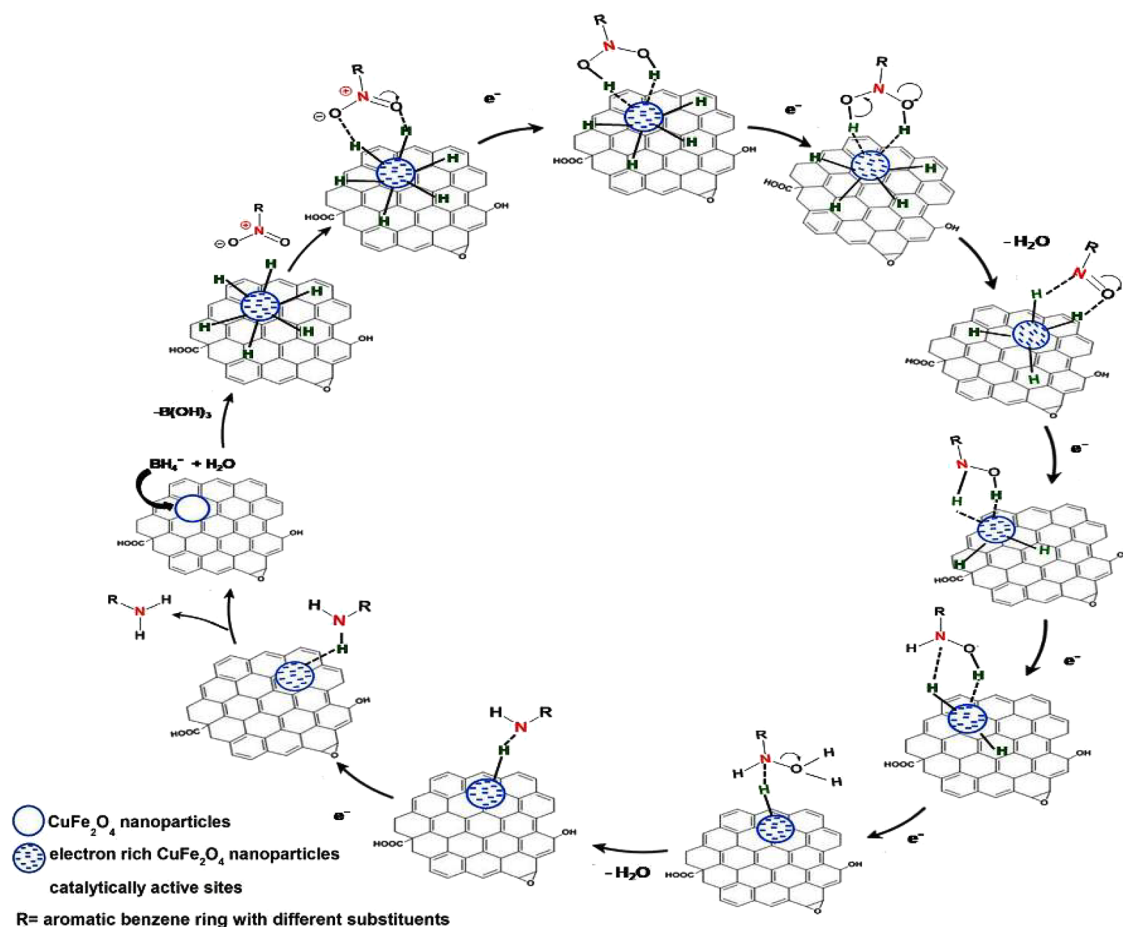
Figure 2. Changes in the time-dependent UV–Vis spectra of (a) 2-nitrophenol (2-NP), (b) pseudo-first-order kinetics plot of the reduction reaction of different nitroaromatic compounds with CuFe₂O₄-rGO, and (c) depiction of magnetic separability of the catalyst by a permanent magnet from the reaction mixture.

publication, we have reported the synthesis of the CuFe₂O₄-rGO nanocomposite.¹⁵ Scheme 1 illustrates the preparation of the CuFe₂O₄-rGO nanocomposite. Here, chloride salts of Cu²⁺ and Fe²⁺ were used as starting materials for the formation of CuFe₂O₄-rGO nanocomposites. In this synthesis, the formation of rGO via reduction of GO and the formation of CuFe₂O₄ nanoparticles occurred simultaneously. Here, NaOH played a dual role: (i) acting as a reducing agent to convert GO to rGO and (ii) acting as a precipitating agent for Cu²⁺ and Fe³⁺ during the formation of CuFe₂O₄ nanoparticles under coprecipitation reaction conditions. PEG acts as a capping agent and prevents the formation of large particles or agglomeration of CuFe₂O₄ nanoparticles during the formation of CuFe₂O₄, and the following reactions might have occurred (eqs 1–3).^{27,28} A detailed protocol for the synthesis of the CuFe₂O₄-rGO nanocomposite is provided in the Supporting Information.



The structures of the synthesized CuFe₂O₄-rGO nanocomposite, pure GO, and pure rGO were examined by using XRD, FESEM, EDS, FT-IR, and Raman spectroscopy. Figure 1a corresponds to the XRD spectra of GO, CuFe₂O₄, and CuFe₂O₄-rGO nanocomposites. The diffraction peaks at 9.76° and 42.14° corresponding to (001) and (101) planes respectively correspond to the diffraction pattern of pure GO.¹² In the XRD diffractogram of CuFe₂O₄ and CuFe₂O₄-rGO, peaks at 2θ = 18.16°, 30.11°, 35.62°, 37.36°, 39.01°, 43.27°, 57.46°, and 62.72° referring to (111), (220), (311), (202), (222), (400), (511), and (440) planes of the cubic crystal of CuFe₂O₄ (JCPDS card no. 77-0010) were observed.^{27,29,30} This fact highlighted the presence of CuFe₂O₄ nanoparticles in CuFe₂O₄-rGO nanocomposites. Also, the characteristic peaks of GO (i.e., 2θ = 9.76° and 42.14°) are absent in the XRD pattern of CuFe₂O₄-rGO, indicating the conversion of GO to rGO during the formation of CuFe₂O₄-rGO nanocomposites.¹⁵

Scheme 2. Plausible Mechanism of Reduction of Nitroaromatic Compounds by a CuFe_2O_4 -rGO Nanocomposite in the Presence of Excess NaBH_4



Raman spectra of GO, rGO, and CuFe_2O_4 -rGO composites are provided in Figure 1b. In the Raman spectra, the characteristic bands at 1345 and 1587 cm^{-1} representing D and G bands of pure GO were observed, whereas for rGO, the distinctive D and G bands were obtained at 1328 and 1580 cm^{-1} , respectively. In the case of CuFe_2O_4 -rGO, the D and G bands appeared at lower values, i.e., 1332 and 1572 cm^{-1} , respectively, with respect to GO. This is due to the reduction of GO to rGO.^{31,32} For GO, the value of I_D/I_G was ~ 0.9 , whereas for rGO and CuFe_2O_4 -rGO, the ratios were ~ 1.04 and ~ 1.02 , respectively. This rise in I_D/I_G value for rGO and CuFe_2O_4 -rGO is attributed to the emergence of more defects in the samples on the reduction of the average size of sp^2 domains during the formation of CuFe_2O_4 -rGO composites.^{15,33,34}

In the FT-IR spectra of GO (Figure S1), the peaks at 1232, 1728, 1382, and 1056 cm^{-1} indicated the presence of an epoxy group, carbonyl group, carboxylic group, and C–O stretching vibration on the surface of GO, respectively. Also, the peak at 1621 cm^{-1} corresponds to the skeletal vibration of the graphitic domains.^{35,36} Moreover, the vanishing of the peaks at 1728 and 1231 cm^{-1} and the diminishing intensity of the peak at 1382 cm^{-1} specified the reduction of oxygen-bearing groups of GO during the formation of CuFe_2O_4 -rGO nanocomposites. This fact indicated the conversion of GO to rGO during this process. A band at 594 cm^{-1} was also observed in the spectra of CuFe_2O_4 -rGO, which can be

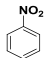
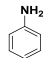
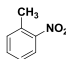
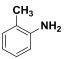
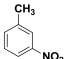
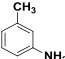
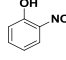
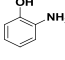
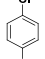
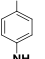
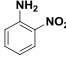
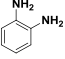
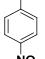
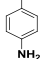
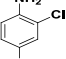
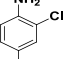
ascribed to the lattice absorption of M–O (M = Fe^{3+} and Cu^{2+}), indicating the formation of CuFe_2O_4 .^{15,37}

Figure 1c presents the FESEM image of this nanocomposite, illustrating the immobilization of CuFe_2O_4 nanoparticles on the surface of nanometer-thin rGO sheets. The composition of the nanocomposite containing Cu, Fe, and C is revealed through the EDS analysis (Figure S2).

2.2. CuFe_2O_4 -rGO-Catalyzed Reduction Reaction of Nitroaromatic Compounds: Kinetics and Reaction Mechanism.

Our previous study demonstrated that CuFe_2O_4 -rGO can act as an efficient catalyst for the reduction of 4-nitrophenol to 4-amino phenol in an aqueous medium.¹⁵ In this present study, we have explored the catalytic efficiency of CuFe_2O_4 -rGO for the reduction of various nitroaromatic compounds and investigated the kinetics of the reduction reactions. The progress of reaction with time was tracked by using UV–Vis spectroscopy. As a representative, the time-dependent UV–Vis spectra of the CuFe_2O_4 -rGO-catalyzed reduction of 2-nitrophenol (2-NP) to 2-aminophenol (2-AP) are presented in Figure 2, and the UV–Vis spectra of other nitroaromatic compounds are shown in Figures S3 and S4. In the UV–Vis spectra, the absorption maxima (λ_{max}) at 354 nm are observed for the aqueous solution of 2-NP, and this peak was shifted to 416 nm after the addition of NaBH_4 due to the phenolate ion formation and the color of the solution changed from pale yellow to dark yellow. To determine the kinetics of this reaction, we have monitored the decline of this peak at 416 nm with the progress of the reaction. As the reaction

Table 1. Apparent Rate Constants of the Reduction Reactions of Various Nitroaromatic Compounds^a

Sr. No.	Starting Material	Product	Apparent Rate constant (min ⁻¹) (k_{app})
1			0.574
2			1.205
3			0.802
4			1.420
5			0.477
6			1.004
7			1.624
8			1.743

^aReaction conditions: [nitro aromatic compounds] = 9×10^{-2} mM (4.5 mL), catalyst dose = 0.1 g L⁻¹, [NaBH₄] = 0.2 M (1 mL), aqueous medium, room temperature.

proceeded, a new peak appeared ($\lambda_{max} = 293$ nm), which indicated the gradual formation of 2-AP. This reduction of 2-NP to 2-AP was completed in 2 min when catalyzed by CuFe₂O₄-rGO. It was noticed that CuFe₂O₄-rGO acted as a very efficient catalyst, and the time required to complete the reduction reactions was varying only from 2 min to 6 min, depending upon the substitution groups present in the aromatic benzene ring of the nitro compounds. Table S1 lists the completion time of reduction of nitroaromatic compounds to the corresponding amino compounds when various catalysts were used. The catalytic efficiency of the synthesized catalyst (CuFe₂O₄-rGO) was found to be significantly superior to the variously reported catalysts. CuFe₂O₄-rGO also showed its catalytic efficiency to reduce trifluralin, which is a toxic herbicide, to its corresponding amine derivative in the aqueous medium (Figure S5).

The plausible reaction mechanism is displayed in Scheme 2. In the preliminary stage of the reaction, BH₄⁻ ions are adsorbed on the surface of the catalyst (CuFe₂O₄-rGO). Then, electron transfer occurs from BH₄⁻ to the CuFe₂O₄ nanoparticles, which generates active hydrogen atoms and leads to the reduction of the nitro group of 2-NP to 2-AP.³⁸ This electron transfer-induced hydrogenation is a spontaneous process where the CuFe₂O₄ nanoparticles play the role of electron storage from the hydride ions and act as catalytically active sites. The presence of rGO enhances the catalytic activity of the catalyst (CuFe₂O₄-rGO) as rGO provides a high surface area for the adsorption of 2-NP and its conducting nature expedites the electron transfer to 2-NP via electrostatic

interaction. The reduction of 2-NP to 2-AP is a six-electron transfer process and proceeds via the formation of several intermediates, such as 2-nitrophenol → 2-nitrosophenol → 2-hydroxyaminophenol → 2-aminophenol.¹⁰ As in the reduction reaction, the attack of H species to the -NO₂ group of the reactant molecule and the electron transfer process lead to the formation of -NH₂ groups, and the electron density of the carbon of benzene, which is attached with the -NO₂ group, plays a critical role. The electron density of this C atom depends upon the nature and position of substituent groups attached to the benzene ring. To determine the effect of the substituent groups on the kinetics of the reduction reaction, we have performed the reaction with various nitroaromatic compounds. As reported by several researchers, this reaction follows the pseudo-first-order kinetics.^{18,19,39} We have determined the apparent rate constants of this reaction by using a pseudo-first-order rate equation (Figure 2b). The apparent rate constants (k_{app}) of the various nitroaromatic compounds are listed in Table 1, which clearly shows the effect of substituent groups on the rate of the reactions. The presence of an electron-donating group (such as -OH, -CH₃, and -NH₂) in nitrobenzene enhances the k_{app} values compared to nitrobenzene. For example, the rate constant of 4-amino nitrobenzene (1.624 min⁻¹) is appreciably higher than that of nitrobenzene (0.574 min⁻¹), whereas the presence of an electron-withdrawing group, such as -Cl, causes a decrease in the rate constant (0.477 min⁻¹). Moreover, the position of the substituent groups also affects the rate constant. The higher value of k_{app} of 4-amino nitrobenzene (1.624 min⁻¹) than that

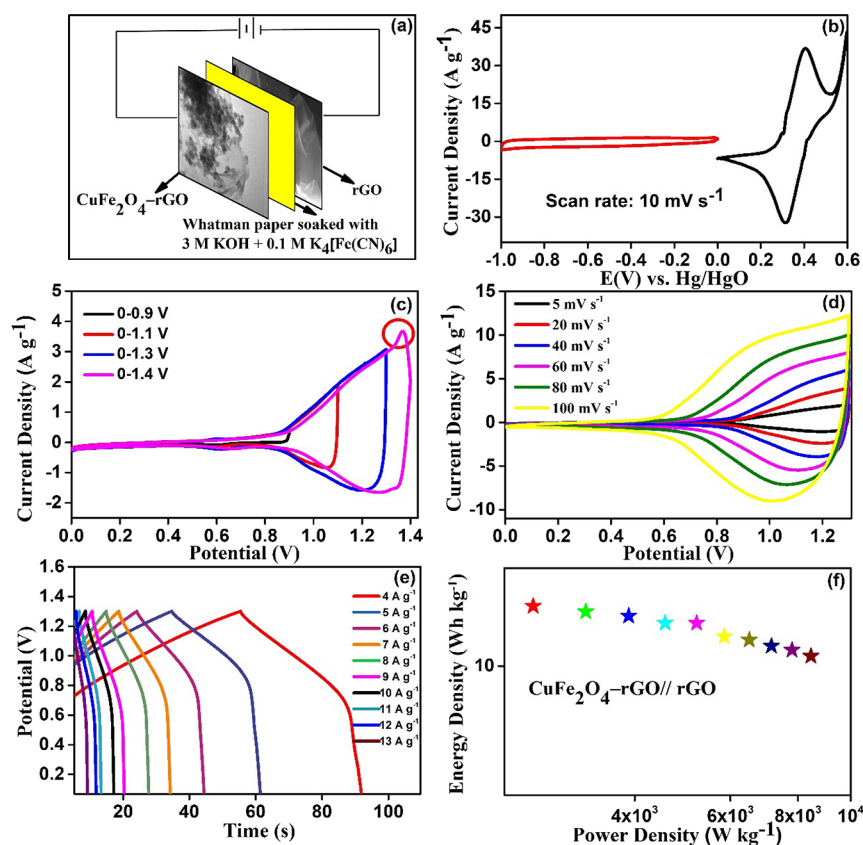
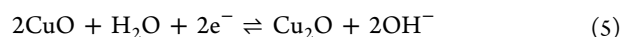
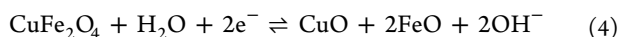


Figure 3. (a) Schematic demonstration of an ASC cell, (b) CV curves of pure rGO and $\text{CuFe}_2\text{O}_4\text{-rGO}$ recorded in a three-electrode setup, (c) CV profiles of ASC at 10 mV s^{-1} in varying potential windows, (d) CV profiles at varying sweep rates, (e) GCD curves at varying current densities, and (f) Ragone plot for an asymmetric setup.

of 2-nitrobenzene (1.004 min^{-1}) indicates the effect of the steric effect on the rate of the reaction.

2.3. Magnetic Separability and Recyclability. We have exploited the magnetic character of the $\text{CuFe}_2\text{O}_4\text{-rGO}$ nanocomposite (saturation magnetization $M_s = 12 \text{ emu g}^{-1}$) to recover this catalyst after the completion of the reaction.¹⁵ Figure 2c demonstrates that the catalyst can easily be recovered from the reaction mixture after completion of the reaction by simply placing a permanent magnet (N35-grade NdFeB magnet having an energy product $\text{BH}_{\text{max}} = 33\text{--}36 \text{ MGOe}$) on the outside wall of the reaction vessel.¹⁵ After recovery, the catalyst was used for the next cycle and we have observed that the $\sim 92\text{--}95\%$ catalysis efficiency of the catalyst was retained even after the fifth cycle of the catalysis reaction.

2.4. Electrochemical Measurements. In our previous study, the electrochemical performances of $\text{CuFe}_2\text{O}_4\text{-rGO}$ have been evaluated by constructing a three-electrode setup (employing $\text{CuFe}_2\text{O}_4\text{-rGO}$ as the working electrode and an Ag/AgCl electrode and a Pt wire as the reference electrode and counter electrode, respectively), which showcased the pseudocapacitive character of $\text{CuFe}_2\text{O}_4\text{-rGO}$ in aqueous 3 M KOH electrolyte.¹⁵ The pseudocapacitive nature of CuFe_2O_4 has been reported by several researchers.^{27,40,41} In the alkaline electrolyte system, CuFe_2O_4 generally shows the Faradaic reactions in the positive potential range, and the redox reactions originate from the intervalence charge transfer between $\text{Cu}^{2+}/\text{Cu}^+$ and $\text{Fe}^{3+}/\text{Fe}^{2+}$. The redox reactions can be presented as eqs 4 and 5.^{15,42–44}



A pair of cathodic/anodic peaks (0.35/0.48 V) in the CV profile of $\text{CuFe}_2\text{O}_4\text{-rGO}$ originates from these redox reactions of CuFe_2O_4 and indicates its pseudocapacitive nature (Faradaic behavior).

Moreover, the alike nature of these peaks suggested the reversibility of the electrochemical reaction occurring on the electrode's surface.

Further, we have observed that the specific capacitance (C_s) of $\text{CuFe}_2\text{O}_4\text{-rGO}$ has enhanced outstandingly from 313 to 797 F g^{-1} at 2 A g^{-1} on the addition of 0.1 M $\text{K}_4[\text{Fe}(\text{CN})_6]$ solution to 3 M KOH.¹⁵ This intensification of C_s happened because of the addition of $\text{K}_4[\text{Fe}(\text{CN})_6]$, where $[\text{Fe}(\text{CN})_6]^{4-}/[\text{Fe}(\text{CN})_6]^{3-}$ acted as an electron buffer source, hence offering an additional redox reaction in the electrochemical phenomenon occurring at the electrode/electrolyte interface.^{45–48} Therefore, the present study involves the use of an aqueous mixture of 3 M KOH and 0.1 M $\text{K}_4[\text{Fe}(\text{CN})_6]$ as the electrolyte system.

2.4.1. Electrochemical Performances of an Asymmetric Supercapacitor (ASC Device). In the present work, to pull off impressive energy density and power density, an asymmetric supercapacitor (ASC) cell was devised, employing $\text{CuFe}_2\text{O}_4\text{-rGO}$ as a cathode and rGO as an anode. Figure 3a portrays the schematic diagram of an asymmetric cell. Figure 3b exhibits the CV profiles of $\text{CuFe}_2\text{O}_4\text{-rGO}$ and rGO electrodes at 10 mV s^{-1} scan rate, recorded from the three-electrode setup in working potential ranges of 0 to 0.6 V and -1 to 0 V, respectively. The rationality of the pseudocapacitive nature of $\text{CuFe}_2\text{O}_4\text{-rGO}$

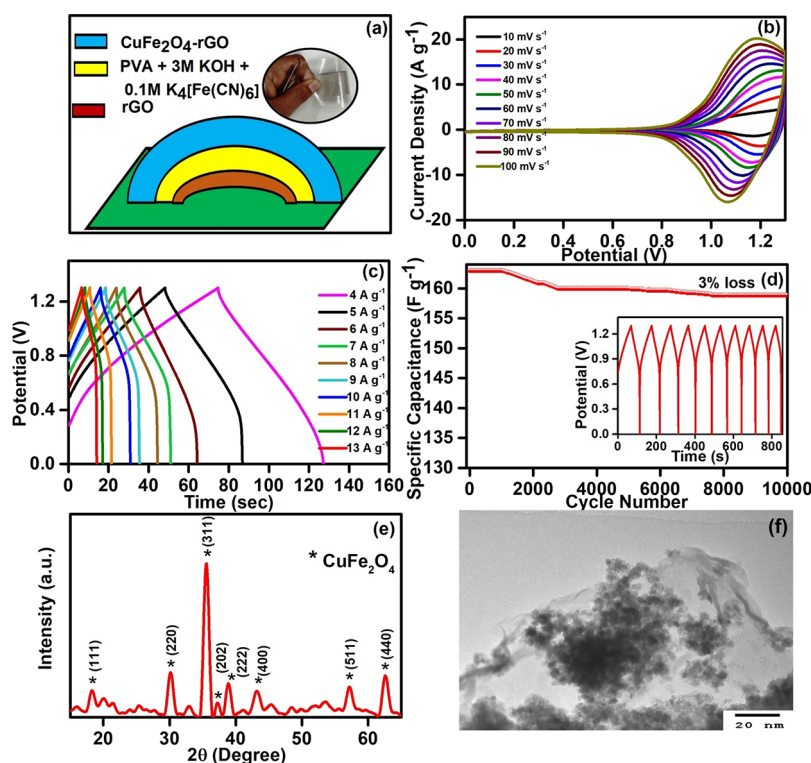


Figure 4. (a) Depiction of a flexible ASC model, (b) CV curves at full scan rate, (c) GCD curves at varying current densities, (d) cycling life performance (inset: GCD curves of 10 cycles after 5000 cycles), and (e) XRD pattern and (f) TEM image of a CuFe_2O_4 -rGO electrode material after 10,000 charge–discharge cycles.

and the EDLC nature of pure rGO are proved by the shape of the CV curves. Figure 3c portrays the CV profiles in varying potentials at a sweep rate of 10 mV s^{-1} . The rise in the current and area under the CV curves on the extension of the window up to 1.3 V proved the feasibility of this voltage window for the ASC device. Further, it was also noticed that when the working potential was stretched beyond 1.4 V, the CV curve exhibits an unwanted peak due to oxygen emergence. Figure 3d represents the CV profiles obtained at varying sweep rates from 10 to 100 mV s^{-1} . The well-retained CV profile even with rising scan rate and the nearly symmetric triangular shape of the GCD curves indicated the good rate performance and balanced charge storage with remarkable electrochemical reversibility (Figure 3e).^{8,48} The C_S value obtained from the GCD measurements was 113 F g^{-1} at a current density of 4 A g^{-1} , and it was observed that the C_S value declined with rising current density. This is due to the depressed ion penetration at comparatively higher current densities, causing incomplete redox reaction at the electrode surface/electrolyte interface.

Energy density and power density, being the pivotal parameters of the ASC device, were calculated from the GCD measurements and correlated through the Ragone plot. This CuFe_2O_4 -rGO//rGO ASC device delivered a high energy density of $\sim 26 \text{ Wh kg}^{-1}$ at a power density of 2600 W kg^{-1} in an aqueous electrolyte (3 M KOH + 0.1 M $\text{K}_4[\text{Fe}(\text{CN})_6]$). This energy density is remarkably higher than that of literature-reported values as well as that of a commercial supercapacitor ($3\text{--}9 \text{ Wh kg}^{-1}$ at $3000\text{--}10,000 \text{ W kg}^{-1}$).^{48–50}

2.4.2. Electrochemical Performances of the Mechanically Flexible All-Solid-State ASC Device. Since the CuFe_2O_4 -rGO//rGO ASC device exhibited its excellent energy harvesting ability with a high burst of power supply, an effort has been made to fabricate flexible supercapacitors with exceptional

electrochemical performance. The method of fabrication of this flexible all-solid-state ASC device has been addressed in Section 4, and the schematic illustration is portrayed in Figure 4a. CV and GCD measurements were carried out in 0 to 1.3 V potential to calculate the C_S , energy density, and power density of this flexible ASC device. Figure 4b delineates the CV curves at varying scan rates from 10 to 100 mV s^{-1} in a potential window of 0–1.3 V. The CV curves of the flexible ASC device maintained almost the same shape even at the high scan rate up to 100 mV s^{-1} . Also, the C_S values obtained from the GCD curves at varying current densities are shown in Figure 4c. The maximum C_S value of 163 F g^{-1} was obtained at a current density of 4 A g^{-1} , and the C_S values were found to be lowered with rising current densities. A Nyquist plot (Figure S6) was obtained from EIS measurements to investigate the ion transport mechanism. The fabricated flexible ASC device evinced the values of 0.71Ω and 0.85Ω for R_{ct} (charge transfer resistance) and R_s (equivalent series resistance), respectively. The fitting parameters are listed in Table S2. The cycling life test was conducted at a current density of 2.5 A g^{-1} for this flexible all-solid-state ASC device, and it is shown in Figure 4d. This device exhibited remarkable shelf-life by retaining $\sim 97\%$ of the initial C_S even after 10,000 cycles. This superb cycling stability can be explained from the powder XRD and FESEM analysis of the electrode material obtained from the electrode after repeated charge–discharge cycles. The absence of any additional diffraction peak in the XRD pattern confirmed the phase stability of the collected material (Figure 4e). Also, the TEM micrograph (Figure 4f) divulged no significant change in the microstructure. These results indicated the stability of CuFe_2O_4 -rGO during the electrochemical phenomenon in the presence of an alkaline electrolyte.

Figure 5a represents the Ragone plot, which correlates the energy and power density derived from GCD measurements

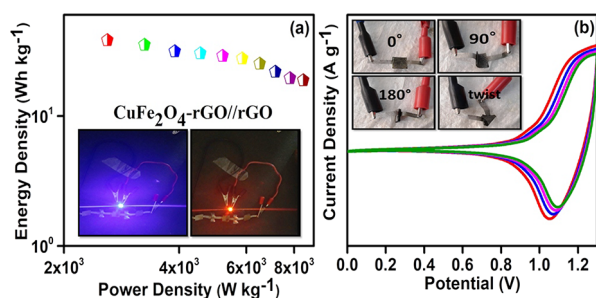


Figure 5. (a) Ragone plot for a $\text{CuFe}_2\text{O}_4\text{-rGO//rGO}$ flexible asymmetric device representing the high energy efficiency of the device by lightening up the blue and red LEDs and (b) CV scans recorded at multiple bending states of 0° , 90° , and 180° and the twisted state.

for this flexible all-solid-state ASC device. The energy density of the fabricated device could realize a high value of 38 Wh kg^{-1} at a power density of 2600 W kg^{-1} in an aqueous electrolyte. These results are superior to many previous findings as well as supercapacitors available in the market for commercial purposes. To explore the practical applicability of the fabricated all-solid-state flexible asymmetric device, the three devices were connected in series and successfully lightened up the LEDs shown in Figure 5a, inset.

To demonstrate the bendability of this all-solid-state ASC device, the device was put through varying bending deformations of 0° , 90° and 180° and the twisted state, and it is shown in Figure 5b, inset. CV profiles were recorded at different bending positions and nearly overlapping CV curves were obtained, endowing the negligible recession on the C_s of this device on bending, thus exhibiting its mechanical pliability.

In this $\text{CuFe}_2\text{O}_4\text{-rGO}$ nanocomposite, CuFe_2O_4 offers a rich Faradaic redox reaction and rGO provides a support framework with a high surface area and electric conductivity.¹⁵ The synergistic effect, originating from the intertwining existence of CuFe_2O_4 nanoparticles and rGO in the nanocomposite, persuades speeding up of the electrochemical process and catalytic reduction reaction by accelerating the electron transport by contracting the transportation length of the ions in the hierarchical nanostructure. Hence, $\text{CuFe}_2\text{O}_4\text{-rGO}$ nanocomposites demonstrated great supercapacitive performance and excellent catalytic property.

3. CONCLUSIONS

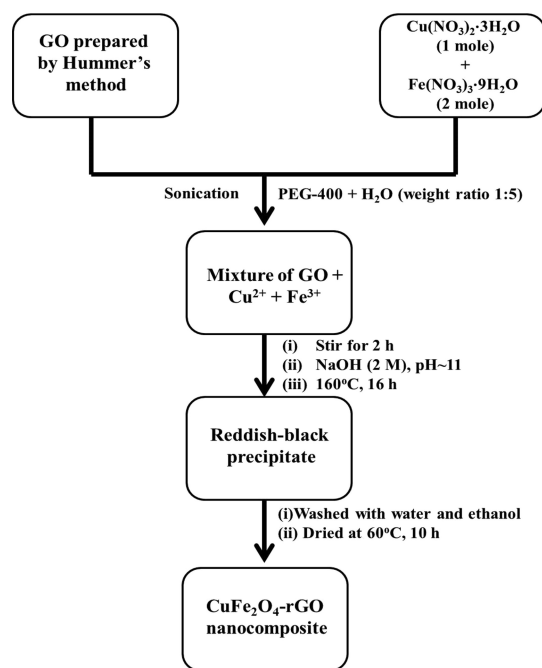
In the current work, we have endorsed the multifunctional disposition of the $\text{CuFe}_2\text{O}_4\text{-rGO}$ nanocomposite where CuFe_2O_4 nanoparticles are docked on the surface of nanometer-thin rGO sheets. A fascinating composition and morphological architecture of this nanocomposite were elicited in two different applications: (i) a high-performance flexible all-solid-state asymmetric supercapacitor device was fabricated by employing this nanocomposite as the cathode and pure rGO as the anode. The fabricated device ($\text{CuFe}_2\text{O}_4\text{-rGO//rGO}$) displayed a high C_s value (163 F g^{-1} at a current density of 4 A g^{-1}) along with a stable cycling life (10,000 cycles). The high energy density (38 Wh kg^{-1}) and power density (2600 W kg^{-1}) of this supercapacitor device advocate in favor of its candidature in suitable energy storage technology. The

distinguished mechanical flexibility along with sustainable cell performance under various bending deformities is an exclusive facet of this device. (ii) The catalytic efficiency of this nanocomposite toward the reduction reaction of a variety of nitroaromatic compounds to their amino derivatives was also appraised, which clearly illustrated that its catalytic performance is superior to many of the reported catalysts (Table S1). This catalyst was betrothed to reduce trifluralin, which is a herbicide and a water pollutant, to its amine form. Moreover, the easy magnetic recovery process is supplemental leverage of the catalyst. These astonishing performances make $\text{CuFe}_2\text{O}_4\text{-rGO}$ a fascinating nanocomposite.

4. EXPERIMENTAL SECTION

4.1. Synthesis of $\text{CuFe}_2\text{O}_4\text{-rGO}$. An “in situ” coprecipitation reduction synthesis route was adopted for synthesizing $\text{CuFe}_2\text{O}_4\text{-rGO}$ nanocomposites.¹⁵ The steps involved in the synthesis of the $\text{CuFe}_2\text{O}_4\text{-rGO}$ nanocomposite is presented in Scheme 1, and a flowchart illustrating the stepwise synthesis route is presented in Scheme 3. The details of the synthesis protocol are provided in the Supporting Information.

Scheme 3. Schematic Presentation of the Synthesis of the $\text{CuFe}_2\text{O}_4\text{-rGO}$ Nanocomposite



4.2. Characterization. The synthesized materials were analyzed by X-ray diffraction (XRD), Fourier transform-infrared spectroscopy (FT-IR), field emission scanning electron microscopy (FESEM), energy dispersive spectra analysis (EDS), Raman spectroscopy, and UV–Vis spectroscopy. The details about the chemicals and the instrumentation facility are documented in the Supporting Information.

4.3. Catalytic Activity Tests. **4.3.1. Reduction of Nitroaromatic Compounds.** Reduction of nitroaromatic compounds was performed in excess NaBH_4 by using the $\text{CuFe}_2\text{O}_4\text{-rGO}$ nanocomposite. The progression of the reduction reaction was tracked by recording the absorbance spectra by a UV–Vis spectrophotometer at regular time

intervals. The protocol for carrying out the reduction reaction is provided in the [Supporting Information](#).

4.3.2. Magnetic Separability. After finishing the catalysis reaction, the catalyst was magnetically retrieved by placing a permanent magnet (N35-grade NdFeB magnet having an energy product $BH_{\max} = 33\text{--}36$ MGOe) on the outside of the reaction vessel.¹⁵ After the complete retraction of all the catalyst nanoparticles by the magnet, the reaction mixture was separated from the vessel. After recovery, the catalyst was washed with water followed by ethanol and then dried in a vacuum oven at 70 °C overnight. After drying, the catalyst was used for the next cycle.

4.4. Electrochemical Measurements. In our previous paper, we have described the details of the electrochemical measurements (CV, GCD, and EIS) in a three-electrode setup,¹⁵ where $\text{CuFe}_2\text{O}_4\text{-rGO}$, Hg/HgO electrode, and a Pt wire were used as the working electrode, reference electrode, and counter electrode, respectively. In the present work, we have constructed the two-electrode setup in the form of an asymmetric device and carried out the electrochemical measurements (CV, GCD, and EIS) to access the electrochemical performances (C_s , power density, energy density, and cycle life) of these devices. The details of the fabrication of the asymmetric devices are provided in the next section ([Section 4.5](#)). For the electrochemical measurements, a workstation IVIUMSTAT (10/5A/8 MHz) was used. CV measurements were performed in a voltage window of 0–1.3 V and at different scan rates ranging from 10 to 100 mV s^{-1} . GCD measurements were performed at varying current densities ranging from 4 to 13 A g^{-1} at a potential window of 0–1.3 V. To measure the cyclic stability of the device, GCD measurements were carried out for 10,000 cycles using a potential window of 0–1.3 V and a current density of 2.5 A g^{-1} . Electrochemical impedance spectroscopy (EIS) measurements were performed in the frequency range of 0.01–10,000 Hz using an alternating current amplitude of 0.01 V.

To establish the mechanical flexibility of the fabricated all-solid-state ASC device, its electrochemical performances were measured at different bending conditions (90°, 180°, and twisted) using the aforementioned measurement parameters. The equations for calculating the C_s , power density, and energy density are provided in the [Supporting Information \(eqs S3–S5\)](#).

4.5. Fabrication of Supercapacitor Devices. **4.5.1. Construction of an Asymmetric Supercapacitor (ASC) Cell.** To construct an ASC cell, $\text{CuFe}_2\text{O}_4\text{-rGO}$ and pure rGO were assigned as positive and negative electrodes, respectively, and Ni foam was used as an electron collector. The method of electrode preparation is presented in the [Supporting Information](#). The amount of active electrode materials required ($\text{CuFe}_2\text{O}_4\text{-rGO}$ for cathode and rGO for anode) for the preparation of these two electrodes was estimated by applying charge balance theory ([eqs S6–S8](#)), and the mass ratio of $\text{CuFe}_2\text{O}_4\text{-rGO}$:rGO used here was 0.5. A Whatman-42 filter paper was used as a separator, which was soaked with the aqueous mixture of 3 M KOH and 0.1 M $\text{K}_4[\text{Fe}(\text{CN})_6]$.

4.5.2. Fabrication of an All-Solid-State Flexible ASC Device. The all-solid-state flexible ASC device was fabricated by applying the PVA gel on the surface of the positive electrode (i.e., $\text{CuFe}_2\text{O}_4\text{-rGO}$) and the negative electrode (i.e., rGO) and placing the electrodes one over the other. The PVA gel contained an aqueous solution of 3 M KOH + 0.1 M $\text{K}_4[\text{Fe}(\text{CN})_6]$ and acted as an electrolyte and separator. Then,

the solidification of the PVA gel was allowed to happen, to obtain a thin layer acting as a sandwich between the two working electrodes.

■ ASSOCIATED CONTENT

Supporting Information

The Supporting Information is available free of charge at <https://pubs.acs.org/doi/10.1021/acsomega.1c03377>.

Synthesis of $\text{CuFe}_2\text{O}_4\text{-rGO}$; chemicals, characterization, and instrumentation; equations and method for electrode preparation for an ASC cell; EDS analysis of a $\text{CuFe}_2\text{O}_4\text{-rGO}$ nanocomposite; FT-IR spectra of GO, rGO, and $\text{CuFe}_2\text{O}_4\text{-rGO}$ nanocomposites; time-dependent UV–Vis spectra of 2-nitrotoluene, 3-nitrotoluene, nitrobenzene, 1-chloro-4-nitrobenzene, 4-nitroaniline, 2-nitroaniline, 2-chloro-4-nitroaniline, and trifluralin decomposition catalyzed by the $\text{CuFe}_2\text{O}_4\text{-rGO}$ nanocomposite; table of comparison for different types of nitroaromatic compounds catalyzed by different catalysts; Nyquist plot and fitting results of the EIS data of an all-solid-state flexible asymmetric ($\text{CuFe}_2\text{O}_4\text{-rGO}/\text{rGO}$) supercapacitor device ([PDF](#))

■ AUTHOR INFORMATION

Corresponding Author

Narendra Nath Ghosh – Nano-materials Lab, Department of Chemistry, Birla Institute of Technology and Science, Pilani K K Birla Goa Campus, Pilani, Goa 403726, India;
orcid.org/0000-0002-8338-7292; Phone: +91 832 2580318/25570339; Email: naren70@yahoo.com

Authors

Priyanka Makkar – Nano-materials Lab, Department of Chemistry, Birla Institute of Technology and Science, Pilani K K Birla Goa Campus, Pilani, Goa 403726, India
Debika Gogoi – Nano-materials Lab, Department of Chemistry, Birla Institute of Technology and Science, Pilani K K Birla Goa Campus, Pilani, Goa 403726, India
Debmalya Roy – Defence Materials and Stores Research & Development Establishment (DMSRDE) DRDO, Ministry of Defence, Government of India, PO DMSRDE, Kanpur 208013, India

Complete contact information is available at:
<https://pubs.acs.org/doi/10.1021/acsomega.1c03377>

Notes

The authors declare no competing financial interest.

■ ACKNOWLEDGMENTS

N.N.G. is thankful to the Central Sophisticated Instrumentation Facility (CSIF) of BITS Pilani K K Birla Goa campus for providing the FESEM Facility and Raman Facility and also to DRDO for providing the funding for the project (ERIP/ER/201803003/M/01/1737).

■ REFERENCES

- (1) Sahoo, P. K.; Kumar, N.; Thiyagarajan, S.; Thakur, D.; Panda, H. S. Freeze-casting of multifunctional cellular 3D-graphene/Ag nanocomposites: synergistically affect supercapacitor, catalytic, and antibacterial properties. *ACS Sustainable Chem. Eng.* **2018**, *6*, 7475–7487.
- (2) Hu, M.; Yao, Z.; Wang, X. Graphene-based nanomaterials for catalysis. *Ind. Eng. Chem. Res.* **2017**, *56*, 3477–3502.

- (3) Shen, T.; Zhao, Z.; Zhong, Q.; Qin, Y.; Zhang, P.; Guo, Z.-X. Preparation of graphene/Au aerogel film through the hydrothermal process and application for H₂O₂ detection. *RSC Adv.* **2019**, *9*, 13042–13047.
- (4) Noori, A.; El-Kady, M. F.; Rahmanifar, M. S.; Kaner, R. B.; Mousavi, M. F. Towards establishing standard performance metrics for batteries, supercapacitors and beyond. *Chem. Soc. Rev.* **2019**, *48*, 1272–1341.
- (5) Shao, Y.; El-Kady, M. F.; Sun, J.; Li, Y.; Zhang, Q.; Zhu, M.; Wang, H.; Dunn, B.; Kaner, R. B. Design and mechanisms of asymmetric supercapacitors. *Chem. Rev.* **2018**, *118*, 9233–9280.
- (6) Borenstein, A.; Hanna, O.; Attias, R.; Luski, S.; Brousse, T.; Aurbach, D. Carbon-based composite materials for supercapacitor electrodes: a review. *J. Mater. Chem. A* **2017**, *5*, 12653–12672.
- (7) Chee, W. K.; Lim, H. N.; Zainal, Z.; Huang, N. M.; Harrison, I.; Andou, Y. Flexible Graphene-Based Supercapacitors: A Review. *J. Phys. Chem. C* **2016**, *120*, 4153–4172.
- (8) Makkar, P.; Ghosh, N. N. High-Performance All-Solid-State Flexible Asymmetric Supercapacitor Device Based on a Ag-Ni Nanoparticle-Decorated Reduced Graphene Oxide Nanocomposite as an Advanced Cathode Material. *Ind. Eng. Chem. Res.* **2021**, *60*, 1666–1674.
- (9) Cao, X.-M.; Sun, Z.-J.; Zhao, S.-Y.; Wang, B.; Han, Z.-B. MOF-derived sponge-like hierarchical porous carbon for flexible all-solid-state supercapacitors. *Mater. Chem. Front.* **2018**, *2*, 1692–1699.
- (10) Makkar, P.; Chandel, M.; Patra, M. K.; Ghosh, N. N. A “One-Pot” Route for the Synthesis of Snowflake-like Dendritic CoNi Alloy-Reduced Graphene Oxide-Based Multifunctional Nanocomposites: An Efficient Magnetically Separable Versatile Catalyst and Electrode Material for High-Performance Supercapacitors. *ACS Omega* **2019**, *4*, 20672–20689.
- (11) Makkar, P.; Ghosh, N. N. Snowflake-Like Dendritic CoNi Alloy-rGO Nanocomposite as a Cathode Electrode Material for an All-Solid-State Flexible Asymmetric High-Performance Supercapacitor Device. *ACS Omega* **2020**, *5*, 10572–10580.
- (12) Moitra, D.; Anand, C.; Ghosh, B. K.; Chandel, M.; Ghosh, N. N. One-dimensional BiFeO₃ nanowire-reduced graphene oxide nanocomposite as excellent supercapacitor electrode material. *ACS Appl. Energy Mater.* **2018**, *1*, 464–474.
- (13) Mevada, C.; Mukhopadhyay, M. Limitations and recent advances in high mass loading asymmetric supercapacitors based on pseudocapacitive materials. *Ind. Eng. Chem. Res.* **2021**, *60*, 1096–1111.
- (14) You, M.; Zhang, W.; Yan, X.; Jiang, H.; Miao, J.; Li, Y.; Zhou, W.; Zhu, Y.; Cheng, X. V₂O₅ nanosheets assembled on 3D carbon fiber felt as a free-standing electrode for flexible asymmetric supercapacitor with remarkable energy density. *Ceram. Int.* **2021**, *47*, 3337–3345.
- (15) Chandel, M.; Moitra, D.; Makkar, P.; Sinha, H.; Hora, H. S.; Ghosh, N. N. Synthesis of multifunctional CuFe₂O₄-reduced graphene oxide nanocomposite: an efficient magnetically separable catalyst as well as high performance supercapacitor and first-principles calculations of its electronic structures. *RSC Adv.* **2018**, *8*, 27725–27739.
- (16) Dey, C.; De, D.; Nandi, M.; Goswami, M. M. A high performance recyclable magnetic CuFe₂O₄ nanocatalyst for facile reduction of 4-nitrophenol. *Mater. Chem. Phys.* **2020**, *242*, 122237.
- (17) Zhuang, Y.-T.; Gao, W.; Yu, Y.-L.; Wang, J.-H. Facile fabrication of three-dimensional porous CuFe₂O₄ cages as highly efficient and recyclable heterogeneous catalyst. *Mater. Des.* **2017**, *130*, 294–301.
- (18) Ramu, A. G.; Salla, S.; Chandrasekaran, S.; Silambarasan, P.; Gopi, S.; Seo, S.-Y.; Yun, K.; Choi, D. A facile synthesis of metal ferrites and their catalytic removal of toxic nitro-organic pollutants. *Environ. Pollut.* **2021**, *270*, 116063.
- (19) Din, M. I.; Khalid, R.; Hussain, Z.; Najeed, J.; Sahrif, A.; Intisar, A.; Ahmed, E. Critical review on the chemical reduction of nitroaniline. *RSC Adv.* **2020**, *10*, 19041–19058.
- (20) Zhao, J.; Yin, J.; Zhong, J.; Jiao, T.; Bai, Z.; Wang, S.; Zhang, L.; Peng, Q. Facile preparation of a self-assembled artemia cyst shell-TiO₂-MoS₂ porous composite structure with highly efficient catalytic reduction of nitro compounds for wastewater treatment. *Nanotechnology* **2020**, *31*, No. 085603.
- (21) Nirumand, L.; Farhadi, S.; Zabardasti, A. Magnetically separable Ag/CuFe₂O₄/reduced Graphene oxide ternary Nanocomposite with high performance for the removal of Nitrophenols and dye pollutants from aqueous media. *Acta Chim. Slov.* **2018**, *65*, 919–931.
- (22) Zeynizadeh, B.; Aminzadeh, F. M.; Mousavi, H. Green and convenient protocols for the efficient reduction of nitriles and nitro compounds to corresponding amines with NaBH₄ in water catalyzed by magnetically retrievable CuFe₂O₄ nanoparticles. *Res. Chem. Intermed.* **2019**, *45*, 3329–3357.
- (23) Fountoulaki, S.; Daikopoulou, V.; Gkizis, P. L.; Tamiolakis, I.; Armatas, G. S.; Lykakis, I. N. Mechanistic studies of the reduction of nitroarenes by NaBH₄ or hydrosilanes catalyzed by supported gold nanoparticles. *ACS Catal.* **2014**, *4*, 3504–3511.
- (24) Göksu, H.; Çelik, B.; Yıldız, Y.; Şen, F.; Kılbaş, B. Superior monodisperse CNT-supported CoPd (CoPd@CNT) nanoparticles for selective reduction of nitro compounds to primary amines with NaBH₄ in aqueous medium. *ChemistrySelect* **2016**, *1*, 2366–2372.
- (25) Göksu, H. Recyclable aluminium oxy-hydroxide supported Pd nanoparticles for selective hydrogenation of nitro compounds via sodium borohydride hydrolysis. *New J. Chem.* **2015**, *39*, 8498–8504.
- (26) Naik, B.; Hazra, S.; Desagani, D.; Ghosh, B. K.; Patra, M. K.; Vadera, S. R.; Ghosh, N. N. Preparation of a magnetically separable CoFe₂O₄ supported Ag nanocatalyst and its catalytic reaction towards the decolorization of a variety of dyes. *RSC Adv.* **2015**, *5*, 40193–40198.
- (27) Zhang, W.; Quan, B.; Lee, C.; Park, S.-K.; Li, X.; Choi, E.; Diao, G.; Piao, Y. One-step facile solvothermal synthesis of copper ferrite-graphene composite as a high-performance supercapacitor material. *ACS Appl. Mater. Interfaces* **2015**, *7*, 2404–2414.
- (28) Sun, Z.; Liu, L.; Jia, D. Z.; Pan, W. Simple synthesis of CuFe₂O₄ nanoparticles as gas-sensing materials. *Sens. Actuators, B* **2007**, *125*, 144–148.
- (29) Li, X.; Lu, D.; Shao, C.; Lu, G.; Li, X.; Liu, Y. Hollow CuFe₂O₄/α-Fe₂O₃ composite with ultrathin porous shell for acetone detection at ppb levels. *Sens. Actuators, B* **2018**, *258*, 436–446.
- (30) Fotukian, S. M.; Barati, A.; Soleymani, M.; Alizadeh, A. M. Solvothermal synthesis of CuFe₂O₄ and Fe₃O₄ nanoparticles with high heating efficiency for magnetic hyperthermia application. *J. Alloys Compd.* **2020**, *816*, 152548.
- (31) Wang, J.; Deng, Q.; Li, M.; Jiang, K.; Zhang, J.; Hu, Z.; Chu, J. Copper ferrites@reduced graphene oxide anode materials for advanced lithium storage applications. *Sci. Rep.* **2017**, *7*, 8903.
- (32) Moitra, D.; Ghosh, B. K.; Chandel, M.; Ghosh, N. N. Synthesis of a BiFeO₃ nanowire-reduced graphene oxide based magnetically separable nanocatalyst and its versatile catalytic activity towards multiple organic reactions. *RSC Adv.* **2016**, *6*, 97941–97952.
- (33) Zhao, Y.; He, G.; Dai, W.; Chen, H. High catalytic activity in the phenol hydroxylation of magnetically separable CuFe₂O₄-reduced graphene oxide. *Ind. Eng. Chem. Res.* **2014**, *53*, 12566–12574.
- (34) Dhanda, R.; Kidwai, M. Magnetically separable CuFe₂O₄/reduced graphene oxide nanocomposites: as a highly active catalyst for solvent free oxidative coupling of amines to imines. *RSC Adv.* **2016**, *6*, 53430–53437.
- (35) Moitra, D.; Chandel, M.; Ghosh, B. K.; Jani, R. K.; Patra, M. K.; Vadera, S. R.; Ghosh, N. N. A simple ‘in situ’ co-precipitation method for the preparation of multifunctional CoFe₂O₄-reduced graphene oxide nanocomposites: excellent microwave absorber and highly efficient magnetically separable recyclable photocatalyst for dye degradation. *RSC Adv.* **2016**, *6*, 76759–76772.
- (36) Moitra, D.; Ghosh, B. K.; Chandel, M.; Jani, R. K.; Patra, M. K.; Vadera, S. R.; Ghosh, N. N. Synthesis of a Ni_{0.8}Zn_{0.2}Fe₂O₄-RGO nanocomposite: an excellent magnetically separable catalyst for dye

degradation and microwave absorber. *RSC Adv.* **2016**, *6*, 14090–14096.

(37) Zhang, Y.; Chen, Y.; Kang, Z.-W.; Gao, X.; Zeng, X.; Liu, M.; Yang, D.-P. Waste eggshell membrane-assisted synthesis of magnetic CuFe_2O_4 nanomaterials with multifunctional properties (adsorptive, catalytic, antibacterial) for water remediation. *Colloids Surf, A* **2021**, *612*, 125874.

(38) Naik, B.; Hazra, S.; Prasad, V. S.; Ghosh, N. N. Synthesis of Ag nanoparticles within the pores of SBA-15: an efficient catalyst for reduction of 4-nitrophenol. *Catal. Commun.* **2011**, *12*, 1104–1108.

(39) Gao, S.; Sui, Y.; Wei, F.; Qi, J.; Meng, Q.; Ren, Y.; He, Y. Dandelion-like nickel/cobalt metal-organic framework based electrode materials for high performance supercapacitors. *J. Colloid Interface Sci.* **2018**, *531*, 83–90.

(40) Israr, M.; Iqbal, J.; Arshad, A.; Sadaf, A.; Rani, M.; Rani, M.; Jabeen, S. $\text{CuFe}_2\text{O}_4/\text{GNPs}$ nanocomposites for symmetric supercapacitors and photocatalytic applications. *J. Phys. D: Appl. Phys.* **2021**, *54*, 395501.

(41) Sharma, V.; Pan, U. N.; Singh, T. I.; Das, A. K.; Kim, N. H.; Lee, J. H. Pragmatically designed tetragonal copper ferrite super-architectures as advanced multifunctional electrodes for solid-state supercapacitors and overall water splitting. *Chem. Eng. J.* **2021**, *415*, 127779.

(42) Zhu, M.; Meng, D.; Wang, C.; Diao, G. Facile fabrication of hierarchically porous CuFe_2O_4 nanospheres with enhanced capacitance property. *ACS Appl. Mater. Interfaces* **2013**, *5*, 6030–6037.

(43) Vidhyadharan, B.; Misnon, I. I.; Abd Aziz, R.; Padmasree, K.; Yusoff, M. M.; Jose, R. Superior supercapacitive performance in electrospun copper oxide nanowire electrodes. *J. Mater. Chem. A* **2014**, *2*, 6578–6588.

(44) Xu, L.; Li, J.; Sun, H.; Guo, X.; Xu, J.; Zhang, H.; Zhang, X. In situ growth of $\text{Cu}_2\text{O}/\text{CuO}$ nanosheets on Cu coating carbon cloths as a binder-free electrode for asymmetric supercapacitors. *Front. Chem.* **2019**, *7*, 420.

(45) Maiti, S.; Pramanik, A.; Mahanty, S. Extraordinarily high pseudocapacitance of metal organic framework derived nanostructured cerium oxide. *Chem. Commun.* **2014**, *50*, 11717–11720.

(46) Maiti, S.; Pramanik, A.; Mahanty, S. Interconnected network of MnO_2 nanowires with a “cocoonlike” morphology: redox couple-mediated performance enhancement in symmetric aqueous supercapacitor. *ACS Appl. Mater. Interfaces* **2014**, *6*, 10754–10762.

(47) Maiti, S.; Pramanik, A.; Mahanty, S. Influence of imidazolium-based ionic liquid electrolytes on the performance of nano-structured MnO_2 hollow spheres as electrochemical supercapacitor. *RSC Adv.* **2015**, *5*, 41617–41626.

(48) Makkar, P.; Ghosh, N. N. Facile synthesis of MnFe_2O_4 Hollow Sphere-Reduced Graphene Oxide Nanocomposites as Electrode Materials for All-Solid-State Flexible High-Performance Asymmetric Supercapacitors. *ACS Appl. Energy Mater.* **2020**, *3*, 2653–2664.

(49) Dhibar, S.; Das, C. K. Silver nanoparticles decorated polypyrrole/graphene nanocomposite: A potential candidate for next-generation supercapacitor electrode material. *J. Appl. Polym. Sci.* **2017**, *134*, 1–14.

(50) Conway, B. E. *Electrochemical Supercapacitors: Scientific Fundamentals and Technological Applications*; 1st ed; Kluwer Academic/Plenum Publishers: New York, 1999.